Geochimica et Cosmochimica Acta 395 (2025) 181–194

Contents lists available at ScienceDirect

Geochimica et Cosmochimica Acta

journal homepage: www.elsevier.com/locate/gca

The role of dissolved sulfide in controlling copper speciation in basaltic melts

Antonio Lanzirotti [a,*], Michelle Muth [b], Elisabet Head [c], Matthew Newville [a], Molly McCanta [d], Paul J. Wallace [e], Zoltan Zajacz [f]

[a] Center for Advanced Radiation Sources, The University of Chicago, Chicago 60637, USA
[b] Department of Earth and Space Sciences, University of Washington, Seattle, WA 98195, USA
[c] Department of Earth Science, Northeastern Illinois University, Chicago, IL 60625, USA
[d] Department of Earth and Planetary Sciences, University of Tennessee, Knoxville, TN 37996, USA
[e] Department of Earth Sciences, University of Oregon, Eugene, OR 97403, USA
[f] Department of Earth Sciences, University of Geneva, Geneva, Switzerland

ARTICLE INFO

Associate editor: Georges Calas

Keywords:
Copper
Spectroscopy
X-ray Absorption
Silicate Melt
Speciation

ABSTRACT

This study evaluates changes in copper (Cu) speciation that occur in sulfate-dominated basaltic and andesitic magmas equilibrated at oxygen fugacities (fO_2's) above the nickel-nickel oxide (NNO) buffer. Cu K-edge microfocused X-ray absorption fine structure spectroscopy (XAFS) data are presented from both natural and synthetic silicate glasses. Natural samples analyzed include olivine-hosted melt inclusions from tephra of mafic cinder cones in the Lassen segment of the Cascade arc (USA) and from the Michoacán-Guanajuato volcanic field (Mexico) as representative samples from melts equilibrated at $fO_2 >$ NNO. A comparison with melts equilibrated at $fO_2 <$ NNO is provided by analysis of olivine-hosted melt inclusions from Kīlauea Volcano. Data are also presented from copper- and sulfur-bearing synthetic hydrous andesitic glasses synthesized over a range of fO_2, from roughly NNO-2 to NNO+2. The Cu spectroscopy data from the natural and synthetic glasses show two dominant Cu species, Cu^{1+} oxides (referred to here as Cu–O) and Cu^{1+} sulfides (referred to here broadly as Cu-S, but not precluding Cu-Fe-S species). The relative proportion of each species present correlates with the relative concentration of dissolved sulfide in the melt. Synthetic sulfur-bearing glasses equilibrated at NNO-1.2 were found to contain exclusively Cu-S species. Sulfur-bearing experimental glasses equilibrated at NNO-0.5 give calculated Cu–O/(Cu–O + Cu-S), defined here as the "Cu–O fraction", of < 0.10, whereas sulfur-bearing glasses synthesized at NNO+0.6 and NNO+1.8 give calculated Cu–O fraction > 0.96. Natural melt inclusions from Lassen and Kīlauea show a bimodal distribution in Cu–O fraction, with overlapping ranges, of 0.14–0.77 for Lassen and 0.18—0.78 for Kīlauea. Michoacán-Guanajuato inclusions yield Cu–O fractions of 0.68–0.91. The difference in the calculated proportions of Cu–O to Cu-S species appear correlated with available sulfide in the melt. As relative S^{2-} concentrations decrease, the dissolved Cu species in the melt evolves from dominantly Cu-S to Cu–O. This includes melts equilibrated at fO_2's where S^{6+} is the dominant S species. At intermediate sulfide abundances both species appear to coexist. Thermodynamic modeling of the Cu speciation in these silicate glasses suggests that speciation of Cu as a $CuFeS_2$ melt species (akin to chalcopyrite or intermediate solid solution) most accurately predicts the measured Cu species. The modeling suggests that a_{FeO} in the silicate melt, fO_2 and melt S^{2-} (expressed as fS_2) are the most important parameters controlling the proportions of Cu–O vs. Cu-S species. Our results provide a new perspective for understanding Cu solubility, transport, and partitioning in magmatic systems.

1. Introduction

Understanding how the speciation of copper (Cu) dissolved in silicate melts changes in response to varying magmatic parameters can provide valuable insight regarding metal solubility and transport. Which Cu species are stabilized in a silicate magma may be influenced by melt

---

* Corresponding author at: Center for Advanced Radiation Sources, The University of Chicago, Chicago, IL 60637, USA.
E-mail address: lanzirotti@uchicago.edu (A. Lanzirotti).

https://doi.org/10.1016/j.gca.2025.02.037
Received 10 July 2024; Accepted 28 February 2025

composition, redox conditions, and magmatic pressures and temperatures, factors that can also influence the Cu concentration and solubility (e.g. Gaetani and Grove, 1997; Holzheid and Lodders, 2001; Ripley et al., 2002; Zajacz et al., 2012, 2013). Melt Cu speciation is also critical to interpreting Cu isotope data from magmatic systems (Chen et al., 2022; Zou et al., 2024).

Studies have shown that in terrestrial basaltic and andesitic melts Cu will predominantly stabilize as monovalent Cu^{1+} (Candela and Holland, 1984; Ripley and Brophy, 1995; Holzheid and Lodders, 2001; Lanzirotti et al., 2019; Liu et al., 2024; Miller et al., 2024). Our previous study (Lanzirotti et al., 2019) of olivine-hosted melt inclusions (MI) from Kīlauea equilibrated at oxygen fugacities (fO_2's) below the nickel-nickel oxide (NNO) buffer showed stabilization of both Cu^{1+}-oxide (Cu–O) and Cu^{1+}-sulfide (Cu-S) species, measured using Cu K-edge X-ray absorption fine structure (XAFS) spectroscopy. The relative proportion of the two species in these Kīlauea glasses appeared to be correlated with total measured sulfur (S) abundance. Cu XAFS showed that Kīlauea MI with total S abundances > 1000 ppm were dominated by Cu-S species, yielding Cu K-edge XAFS spectra similar to that measured for covellite (*CuS*) standards. In Kīlauea MI where S concentrations were < 500 ppm Cu^{1+}-oxide species were found to dominate, while in MI with S abundances between 500 and 1000 ppm both species coexist.

The transition from sulfide (S^{2-}) to sulfate (S^{6+}) in silicate melt is influenced by fO_2, temperature and potentially pressure (Matjuschkin et al., 2016; Nash et al., 2019). Although both S^{2-} and S^{6+} species are found in Kīlauea basaltic melts (Jugo et al., 2010; Lerner, 2020), S^{2-} species dominate (Fig. 1). Largely equilibrated at fO_2's below the NNO buffer, Kīlauea MI typically contain only 5–20 % S^{6+} (Lerner, 2020). By contrast, in arc melts equilibrated at fO_2's > NNO, S^{6+} is often the dominant S species in the silicate liquid (Jugo, 2009; Beermann et al., 2011) and the S solubility of the melt increases significantly as S speciation changes from S^{2-} to S^{6+} dominance. These are redox conditions particularly relevant to arc magmas, with which most porphyry copper deposits are associated.

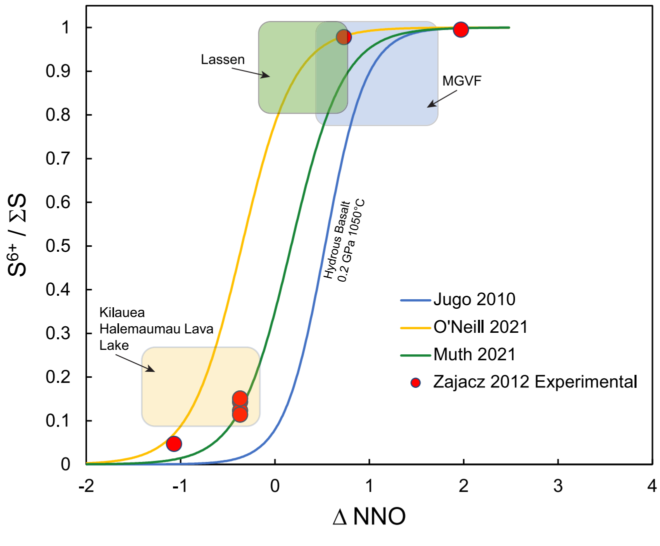

Fig. 1. Comparison of relative fO_2 (ΔNNO) and $S^{6+}/\sum S$ measured in olivine-hosted melt inclusions from the Lassen segment of the Cascade arc and from the Michoacán-Guanajuato volcanic field (Muth and Wallace, 2021, 2022) and from synthetic hydrous synthetic hydrous andesitic glasses (Zajacz et al., 2012) discussed in this paper. Also shown is the fO_2 and $S^{6+}/\sum S$ for melt inclusions from Kīlauea summit eruptions (Lerner, 2020). The curves represent several modeled S – fO_2 redox relationships (Jugo et al., 2010; Muth and Wallace, 2021; O'Neill, 2021) that show the range of fO_2 over which S speciation would be expected to transition from S^{2-} to S^{6+} in basaltic melts. Variations between model curves reflect uncertainties in temperature and/or fO_2 dependence of the speciation (see supplementary material from Muth and Wallace, 2022; Muth and Cottrell, 2023 for detailed discussion).

The solubility of Cu in silicate melts in equilibrium with liquid Cu (Fe) metal and Cu(Fe) sulfide and the partitioning of Cu between silicate melt, silicate minerals, and Cu(Fe) sulfide melt are also influenced by melt fO_2 (Gaetani and Grove, 1997; Holzheid and Lodders, 2001; Ripley et al., 2002; Zajacz et al., 2012; Liu et al., 2014; Miller et al., 2024). It has been hypothesized that the significantly higher S solubility in more oxidized systems (Carroll and Rutherford, 1985; Jugo, 2009) promotes Cu enrichment in the evolving silicate melt. What remains unknown is how the speciation of Cu evolves in these systems as the S content of the melt increases and the sulfur species change from sulfide- to sulfate-dominated.

This study builds on our earlier (Lanzirotti et al., 2019) work and evaluates changes in Cu speciation that occur in sulfate-dominated basaltic and andesitic magmas equilibrated at fO_2's above the NNO buffer. We present direct measurements of Cu speciation in natural and synthetic magmatic glasses, analyzed by Cu K-edge micro-XAFS spectroscopy. Natural samples analyzed include MI hosted in olivine from tephra of mafic cinder cones in the Lassen segment of the Cascade arc, California (USA), and from the Michoacán-Guanajuato volcanic field (MGVF; Mexico). New analyses of olivine-hosted MI from samples collected from the 2008–2018 summit eruptions at Kīlauea Volcano (Thornber et al., 2015), Hawai'i (USA) are also presented, supplementing the data presented in Lanzirotti et al. (2019) and providing a direct comparison to results from the more oxidized Lassen and MGVF systems. Data are also presented from a suite of synthetic hydrous andesitic glasses synthesized at various fO_2's, with geologically-relevant dissolved Cu concentrations (25–265 ppm) and variable S and Cl contents (Zajacz et al., 2012). Since Cu is strongly chalcophile, spectroscopic analysis of synthetic glasses from S-bearing experiments provides more direct constraints on how changes in Cu and S speciation may be coupled in natural silicate melts. In addition to Cu XAFS, the synthetic glasses were also analyzed by S and Cl K-edge micro-XAFS spectroscopy. The Cl K-edge micro-XAFS results are presented in Supplemental Document 1.

2. Methods

2.1. Samples and Preparation

Table 1 lists the natural samples analyzed. These consist of single-side polished, hand-picked grain mounts extracted from specimens of tephra. MI selected for spectroscopic analysis were chosen optically, appeared visibly free of contained quench or daughter crystals and do not contain large or multiple vapor bubbles. Additional details of sample selection and preparation and detailed sampling locations for the Lassen samples are described in the supplemental materials in Muth and Wallace (2021). Sampling locations for the MGVF samples are found in Johnson et al. (2009). The MGVF Electron Probe Micro-Analyses (EPMA), Fourier Transform Infrared (FTIR), and XAFS spectroscopy data presented are newly collected on the tephra samples of Johnson et al. (2009), following the methods of Muth and Wallace (2021). The Kīlauea samples (volcanic glasses collected at the Kīlauea summit vent, Halema'uma'u), and from the East Rift Zone (ERZ) between 2008 and 2018, (Poland et al., 2008; Thornber et al., 2015) were provided by the United States Geological Survey (USGS) Hawaiian Volcano Observatory (HVO) and additional sample details, along with their eruption (and sampling) dates, can be found in Supplemental Table S1.

Table 2 lists the synthetic samples analyzed. These were prepared as part of an earlier study examining the solubility of Au and Cu in hydrous andesite melts and the details regarding starting materials, the quench experiments, and the measured chemical compositions of the run product glasses are fully described in Zajacz et al. (2012).

2.2. Analytical Methods

Microscale XAFS analyses were performed at the GSECARS X-ray

Table 1
Natural MGVF and Lassen glasses analyzed.

Sample ID	Δ NNO[a]	S (ppm)[b]	$S^{6+}/\Sigma S$	est. S^{2-} (ppm)[c]	Cu^{1+}- O fraction[d]	*R-Factor*[e]	Cl (ppm)[b]	FeO^T (wt%) [b]
MGVF								
J1d_m3	+0.99	1650	0.94	99	0.84 (1)	0.0025	1262	6.67
J1d_m4	+1.22	1345	0.95	67	0.83 (1)	0.0017	1248	6.76
ca_a_m13	n/a	831	0.83	141	0.87 (1)	0.0011	931	6.99
ca_a_m7	+0.71	1812	0.96	72	0.68 (1)	0.0034	973	5.73
ca_a_m14	+0.58	1472	0.93	103	0.68 (1)	0.0011	8667	6.51
ca_a_m12	+0.52	1047	0.86	147	0.71 (1)	0.0015	805	6.70
ca_a_m1	+0.64	1043	0.82	188	0.78 (1)	0.0011	1351	7.70
j1d_m20a	n/a	1655	0.96	66	0.71 (1)	0.0022	1179	6.51
j1d_m24	+1.66	1407	0.97	42	0.78 (1)	0.0023	1186	6.69
j1d_m22a	+0.66	1210	0.90	121	0.85 (1)	0.0014	1127	7.24
j1d_m22b	n/a	1259	0.96	50	0.78 (1)	0.0024	1169	6.94
j1d_m23	+1.04	1776	1.00	0	0.82 (1)	0.0036	1256	5.78
j1d_m26	+1.41	1564	0.97	47	0.82 (1)	0.0038	1215	6.65
pada_base_m1	+0.79	1382	0.79	290	0.79 (1)	0.0025	899	6.78
Lassen								
BORG01_02_L1	n/a	994	n/a	n/a	0.65 (1)	0.0027	518	n/a
BORG01-08	n/a	1182	n/a	n/a	0.14 (1)	0.0035	418	n/a
BORG01-09	n/a	1058	n/a	n/a	0.73 (1)	0.0041	574	n/a
BORG01-10	n/a	912	n/a	n/a	0.49 (2)	0.0027	426	n/a
BORG01-11	n/a	1267	n/a	n/a	0.56 (1)	0.0028	387	n/a
BORG01-12	n/a	1134	n/a	n/a	0.15 (2)	0.0041	422	n/a
BORG01-14	n/a	898	n/a	n/a	0.76 (1)	0.0039	458	n/a
BORG01-15	n/a	1336	n/a	n/a	0.75 (2)	0.0048	498	n/a
BORG01-16	n/a	n/a	n/a	n/a	0.14 (2)	0.0034	n/a	n/a
BORG01-19	n/a	966	n/a	n/a	0.72 (1)	0.0047	482	n/a
BORG01-20	n/a	1164	n/a	n/a	0.14 (2)	0.0049	395	n/a
BORG01-21	n/a	874	n/a	n/a	0.74 (1)	0.0034	416	n/a
BORG01-22	n/a	983	n/a	n/a	0.64 (1)	0.0034	562	n/a
BORG01-23	n/a	944	n/a	n/a	0.76 (1)	0.0031	477	n/a
BORG01-24	n/a	894	n/a	n/a	0.67 (1)	0.0032	425	n/a
BORG01-25	n/a	974	n/a	n/a	0.71 (1)	0.0039	534	n/a
BORG01-30	n/a	n/a	0.66	n/a	0.20 (1)	0.0014	n/a	n/a
BORG01-31	+1.30	1508	0.68	483	0.20 (1)	0.0012	591	8.51
BORG01-32	n/a	n/a	n/a	n/a	0.22 (2)	0.0024	n/a	n/a
BORG01-33	n/a	n/a	n/a	n/a	0.62 (2)	0.0033	n/a	n/a
BORG01-34	n/a	n/a	n/a	n/a	0.34 (2)	0.0067	n/a	n/a
BORG01-35	+0.03	1860	0.87	242	0.24 (1)	0.0044	547	7.75
BORG01-37	+0.62	1761	0.90	176	0.25 (2)	0.0049	566	8.17
BORG01-40	+0.37	1197	0.92	96	0.64 (1)	0.0028	560	8.19
BORG01-42	−0.11	1201	0.84	192	0.47 (2)	0.0041	555	7.34
BORG01-43	+0.28	1541	1.01	0	0.28 (2)	0.0047	618	8.1
BORG01-44	+0.46	1595	0.95	80	0.59 (1)	0.0027	563	7.53
BORG01-45	+0.64	1272	1.01	0	0.76 (1)	0.0018	555	8.58
BORG01-47	n/a	n/a	n/a	n/a	0.30 (2)	0.0034	n/a	n/a
BORG01-48	n/a	n/a	n/a	n/a	0.19 (2)	0.0038	n/a	n/a
BORG01-49	n/a	n/a	n/a	n/a	0.66 (1)	0.0091	n/a	n/a
BORG01-50	n/a	n/a	n/a	n/a	0.73 (1)	0.0031	n/a	n/a
BORG01-52	n/a	n/a	n/a	n/a	0.77 (2)	0.0062	n/a	n/a
BORG01-54	n/a	n/a	n/a	n/a	0.15 (2)	0.0038	n/a	n/a
BORG01-55	n/a	n/a	n/a	n/a	0.58 (2)	0.0032	n/a	n/a
BORG01-L17-MM	n/a	1317	n/a	n/a	0.16 (2)	0.0041	546	n/a
Kīlauea								
KS08-07-b-MI	n/a	1216	n/a	n/a	0.29 (1)	0.0024	176	10.56
KS08-07-c-MI1	n/a	1132	n/a	n/a	0.25 (1)	0.0037	88	11.12
KS08-07-c-MI2	n/a	1168	n/a	n/a	0.28 (2)	0.0021	109	10.53
KS08-07-f-MI2	n/a	1276	n/a	n/a	0.28 (2)	0.0024	67	10.88
KS08-07-g-MI	n/a	645	n/a	n/a	0.67 (1)	0.0016	98	11.08
KS08-11-na-MI1	n/a	1158	n/a	n/a	0.25 (2)	0.0075	122	10.59
KS08-11-na-MI2	n/a	1203	n/a	n/a	0.25 (2)	0.0045	105	10.64
KS08-11-nc-MI1	n/a	344	n/a	n/a	0.46 (2)	0.0070	145	9.81
KS08-11-nc-MI2	n/a	719	n/a	n/a	0.78 (2)	0.0038	123	10.65
KS08-11-nd-MI	n/a	1110	n/a	n/a	0.23 (1)	0.0022	107	10.57
KS08-11-ne-MI	n/a	830	n/a	n/a	0.44 (2)	0.0043	135	10.40
KS08-11-nf-MI	n/a	1164	n/a	n/a	0.28 (2)	0.0084	124	10.43
KS08-11-ng-MI	n/a	1183	n/a	n/a	0.18 (1)	0.0022	71	10.72
KS08-108-FD-MI	−1.03	1175	n/a	n/a	0.22 (1)	0.0016	72	11.18
KS08-108-FE-MI	−1.20	1167	n/a	n/a	0.64 (1)	0.0018	107	11.21
KS08-112–12-MI	−1.14	1173	n/a	n/a	0.21 (1)	0.0013	111	11.19
KS08-112–16-MI	n/a	1094	n/a	n/a	0.21 (2)	0.0010	208	10.97
KS08-112–17-MI	n/a	903	n/a	n/a	0.42 (1)	0.0014	132	10.77
KS09-152H-2 W-MI	n/a	813	n/a	n/a	0.73 (2)	0.0031	103	10.78

(*continued on next page*)

Table 1 (*continued*)

Sample ID	Δ NNO^a	S (ppm)^b	$S^{6+}/\Sigma S$	est. S^{2-} (ppm)^c	Cu^{1+}- O fraction^d	*R-Factor*^{e}	Cl (ppm)^b	FeO^T (wt%) ^{b}
KS09-152H-4 W-MI	n/a	685	n/a	n/a	0.63 (1)	0.0018	100	10.84
KS09-152H-3-MI	−0.81	1076	n/a	n/a	0.27 (1)	0.0021	121	10.84
KS09-152-FA-MI	0.10	728	n/a	n/a	0.65 (1)	0.0016	137	11.03
KS10-179H-FA-MI	n/a	498	n/a	n/a	0.75 (1)	0.0015	193	11.17
KS13-267-FA-MI1	−1.86	430	n/a	n/a	0.76 (1)	0.0012	118	10.72
KS13-267-FA-MI2	−1.55	407	n/a	n/a	0.72 (1)	0.0015	131	10.61
KS14-283-FA-MI1	−1.29	427	n/a	n/a	0.73 (1)	0.0012	74	10.54
KS14-283-FA-MI2	−1.25	309	n/a	n/a	0.75 (1)	0.0010	80	10.97
KS14-283-FA-MI3	−2.09	395	n/a	n/a	0.75 (1)	0.0011	125	10.50
KS14-283-FB-MI1	−2.19	307	n/a	n/a	0.74 (1)	0.0010	89	10.67

a: calculated fO_2 as described in Muth and Wallace (2021,2022).
b: chemical compositions from Muth and Wallace (2021, 2022).
c: estimated S^{2-} concentrations based on measured total S abundance and $S^{6+}/\Sigma S$.
d: calculated LCF Cu^{1+}- O fraction with 1σ standard error on fit.
e: calculated residuals (*R-Factor* or fractional misfit) between the fitted and measured spectra of the linear component fitting (LCF) for Cu^{1+}- O fraction. Better fits indicated by lower *R-Factors*.
n/a = not available.

Table 2
Synthetic glasses analyzed.

Sample ID	Δ NNO^a	S (ppm)^b	$S^{6+}/\Sigma S$	est. S^{2-} (ppm)^c	Cu (ppm)^b	Cu^{1+}- O fraction^d	*R-Factor*^{e}	Cl (ppm)^b	FeO^T (wt%)^b
140	−0.5	0	n/a	0	53	0.96 (1)	0.0011	0	5.3
142	−0.5	0	n/a	0	64	0.97 (2)	0.0021	6499	6.2
143	−0.5	0	n/a	0	78	0.90 (1)	0.0030	9974	7.9
155	−0.5	248	0.11	221	45	0.07 (2)	0.0063	0	4.0
156	−0.5	253	0.15	215	54	0.10 (1)	0.0023	1981	5.1
157	−0.5	0	n/a	0	87	0.96 (1)	0.0008	968	5.3
159	−0.5	448	0.12	394	108	0.00 (2)	0.0047	10,280	7.5
160	−0.5	0	n/a	0	77	0.99 (1)	0.0010	516	5.7
161	−0.5	264	0.14	227	66	0.09 (2)	0.0022	1752	4.4
162	0.6	1300	0.98	26	216	1.00 (1)	0.0007	0	5.6
163	−1.2	265	0.05	252	25	0.01 (2)	0.0024	0	4.3
165	1.84	1901	1.00	0	265	0.96 (1)	0.0006	0	5.2

a: calculated fO_2 of run conditions as described in Zajacz et al. (2012). Experiments run at T = 1000 °C, P = 200 Mpa.
b: chemical compositions from Zajacz et al. (2012).
c: estimated S^{2-} concentrations based on measured total S abundance and $S^{6+}/\Sigma S$.
d: calculated LCF Cu^{1+}- O fraction with 1σ standard error on fit.
e: calculated residuals (*R-Factor* or fractional misfit) between the fitted and measured spectra of the linear component fitting (LCF) for Cu(I)- O / Cu(I)- S. Better fits indicated by lower *R-Factors*.
n/a = not available.

microprobe beamline (13-ID-E) at the Advanced Photon Source (APS), Argonne National Laboratory (Argonne, IL USA). Details regarding beamline configuration and instrumentation can be found in Sutton et al. (2022) and Lanzirotti et al. (2019). The Si(111) monochromator crystal set was used for these experiments. Incident beam flux was kept to ~ 2.5e^{10} photons/second for the Cu XAFS analyses and ~ 1.0e^{10} photons/second for the S and Cl XAFS experiments. The focused spot size for this instrument is ~ 2 µm in the horizontal by ~ 1 µm in the vertical (FWHM), but for most of the XAFS analyses presented here the beam was defocused to ~ 10 µm to reduce flux density on the sample and minimize beam induced changes in speciation (see discussions below and in Cottrell et al., 2018; Lerner et al., 2021a). The diameter and thickness of the analyzed MI varies between ~ 50 and 300 µm. All XAFS analytical points within MI were selected following microfocused X-ray fluorescence (XRF) mapping to ensure analysis of homogeneous, inclusion-free glass away from phenocryst and bubble walls.

All XAFS spectra in glasses were collected in fluorescence mode and all XAFS data were corrected for detector dead time and normalized to incident intensity (I_0). When possible, multiple spatially separated points were analyzed (typically between 1 and 5, selected based on XRF compositional mapping) to evaluate compositional homogeneity. These spectra were merged to improve signal quality prior to XAFS analysis.

XAFS spectra were collected with the monochromator scanning energy continuously, with measured intensities binned over given energy intervals. For Cu XAFS, the incident energy was scanned from 8929-8969 eV using 2 eV energy bins, 8969–9009 eV in 0.1 eV bins, and from 9009-9160 eV in 1 eV bins at a scan rate of 3 s per energy bin. A zero valent Cu metal foil standard provided an absorption edge energy of 8980.48 eV, in agreement with refined absorption edge energies measured by Kraft et al. (1996). Spectral overlap from Fe fluorescence background in the measured Cu Kα energy dispersive signal was minimized through addition of a 100 µm aluminum filter between the sample and detector to act as a low energy filter. Repeat measurements of Cu XAFS spectra in selected samples were used to evaluate the potential for beam damage. This testing found no more than 5 % variation in spectral intensities after 60 min of irradiation at the beam conditions described above. The time to collect a single Cu K-edge XAFS spectra with the parameters described is 12 min.

For S XAFS, we used the experimental protocols described in Lerner et al. (2021a) for minimizing and correcting the effects of beam induced changes in measured S XAFS. The incident energy was scanned from 2455-2467 eV using 1.5 eV energy bins, 2467–2485 eV in 0.25 eV bins, and from 2485-2550 eV in 1.0 eV bins at a scan rate of 3 s per energy bin. For Cl XAFS (see Supplemental Document 1), the incident energy was scanned from 2762-2812 eV using 2.0 eV energy bins, 2812–2842 eV in 0.2 eV bins, and from 2842-2978 eV in 2.5 eV bins at a scan rate of 3 s per energy bin. The areas of analysis for Cu, S and Cl XAFS collected in the MI and experimental glasses were selected to try to ensure they did not coincide spatially (again, to minimize beam damage effects).

Bonding material and substrate were analyzed to confirm they contained only trace amounts of Cu and had negligible contribution to the measured MI Cu XAFS signals. Selected olivine hosts were also analyzed to confirm their Cu concentrations are lower than that measured in the MI, so that the contribution to the measured XAFS spectra is negligible (Lanzirotti et al., 2019). Although the bonding materials contain S and Cl, the low penetration and escape depth of the incident and fluorescent X-rays in silicate glass at 2.5 keV (~ 5 μm) make any contribution unlikely. A small subset of the Cu XAFS measured in the Kīlauea natural glasses yielded more sharply-structured spectra suggestive of very fine sulfide quench crystals. These analyses are not included here.

The Larch XAFS analysis software package (Newville, 2013) was used for linear combination fitting (LCF) of the Cu XAFS to quantify the relative proportion of Cu species in the glasses analyzed (Table 1), following the methods described in Lanzirotti et al. (2019). This two-component fitting was done in the normalized μ(E) space over an energy range of 8970 to 9015 eV using edge-normalized Cu K-edge spectra measured in a powdered covellite, *CuS*, standard and an experimental 1-atm Kīlauea tholeiitic basalt (NNO+4.7) glass as the predictor components for Cu-S and Cu–O, respectively.

These two fitting components were chosen on the basis of their similarity to end-member spectra measured in natural glasses (see Lanzirotti et al., 2019 and further discussed below in section 3). The Larch LCF provides the proportions of each Cu species in the fit, which are reported in Tables 1 and 2 in terms of a calculated Cu–O fraction, defined as the LCF Cu–O/(Cu–O + Cu-S) ratio. Repeat fitting shows that the calculated LCF components are typically reproduced to better than 5 %.

Calculated $S^{6+}/\Sigma S$ from measured S XAFS spectra are reported in Tables 1 and 2, quantified using spectral fitting in the Larch XAFS analysis package following the procedures described in Lerner et al. (2021a). This involves fitting of spectral components and absorption peaks, including the spectral backgrounds, that are recognized as corresponding to sulfide complexes, and S^{2-}, S^{4+} and S^{6+} species. LCF fitting then relates the fitted peak areas to $S^{6+}/\Sigma S$ based on calibration to peak intensities measured in experimental hydrous basaltic glasses (Jugo et al., 2010). For glasses with calculated $S^{6+}/\Sigma S$ between 0.07 and 0.85, it is estimated that total accuracy of the S LCF fitting method is better than ± 10 % relative (Lerner et al., 2021a).

Tables 1 and 2 also present measurements of calculated NNO-relative fO_2 and S, Cl and Fe-O^T chemical abundances in the analyzed glasses for comparison. The natural MI for which these data are not available are indicated by "n/a" in the relevant columns of Table 1. The details of how fO_2 were calculated for the Lassen and MGVF samples are described in Muth and Wallace (2021, 2022). Details of wavelength-dispersive EPMA for Fe, S and Cl are also described in Muth and Wallace (2021, 2022). For the synthetic glasses, the fO_2's in Table 2 were calculated based on the experimental run conditions, as described in Zajacz et al. (2012). Details of the EPMA measurements of Fe, S and Cl for these synthetic glasses are also described in Zajacz et al. (2012).

The S, Cl and FeO^T analyses for Kīlauea MI in Table 1 were conducted using a Cameca SX-100, equipped with five wavelength dispersive spectrometers, in the CAMCOR facility at the University of Oregon. The major and minor element compositions were measured in doubly polished MI using 15 kV voltage, a 10 μm beam diameter, and beam currents of 10 and 50nA. In addition, S and Cl concentrations were measured in all glasses following the method of Lerner (2020). Glass and olivine standards were analyzed as unknowns during each run for sample calibration and to assess instrument drift. The NNO-relative fO_2 values for Kīlauea MI in Table 1 are based on major element chemistry measured by EPMA and calculated $Fe^{3+}/\Sigma Fe$ are based on measured Fe K-edge XAFS collected at beamline 13-ID-E, utilizing the Si(311) monochromator crystal set, an ~ 10 μm defocused beam and an incident flux of ~ $5e^{10}$ photons/s. The Fe XAFS analyses in Kīlauea MI follow the analytical protocols described in Lerner et al. (2021a), with $Fe^{3+}/\Sigma Fe$ calculated using the Zhang et al. (2018) calibration on the basis of the measured Fe XAFS pre-edge centroid energy. The fO_2 values were then calculated by applying the Kress and Carmichael (1991) model assuming a melt T of 1150 °C and a pre-eruptive P of 75 MPa (Lerner et al., 2021b).

3. Review of Copper K-edge XAFS Measurements in Basaltic Glasses

Fig. 2 displays Cu K-edge XAFS spectra of selected Cu-bearing reference compounds and synthetic and natural silicate glasses (Lanzirotti et al., 2019). The left plot in Fig. 2 shows XAFS spectra measured in three crystalline Cu^{1+} sulfides, chalcocite (*Cu_2S*), covellite (*CuS*) and chalcopyrite (*$CuFeS_2$*) (Pearce et al., 2006; Goh et al., 2006; Vegelius et al., 2012; Belissont et al., 2016). Also shown is an XAFS spectrum measured in anhydrous *$CuSO_4$*, as representative of XAFS from Cu^{2+}-sulfate species. A key distinguishing feature between Cu^{1+} and Cu^{2+} species is that the spectra for monovalent Cu species typically have an intense low-energy pre-edge peak (peak B) attributed to a 1s → 4p transition, while spectra for Cu^{2+} species display a rising edge position that is at least 2 eV higher in energy (Kau et al., 1987). In crystalline Cu^{1+} species, the intensity of the pre-edge peak correlates with coordination number (Kau et al., 1987). Cu^{2+} complexes generally show a low intensity peak at ~ 8979 eV from 1s → 3d electronic quadrupole transitions, which are typically not observed in Cu^{1+} complexes because of their filled 3d shell (Kau et al., 1987; Fulton et al., 2000).

The Cu^{1+} sulfide mineral standards display subtle spectroscopic differences that are largely reflective of differences in average Cu coordination geometry (Kau et al., 1987; Pearce et al., 2006; Goh et al., 2006). In chalcocite, Cu is thought to largely occupy distorted 3-fold coordinated sites, whereas in chalcopyrite Cu is believed to be primarily tetrahedrally coordinated. In covellite, Cu is considered to occupy a mixture of both tetrahedrally and trigonally coordinated sites. The Cu K-edge XAFS spectra of chalcopyrite and covellite are similar, except that crystalline chalcopyrite displays a more well-resolved pre-edge peak at ~ 8980 eV (peak A) and white-line peak at ~ 8987 eV (peak C), with higher intensities. This pre-edge peak is thought to result from 1s → 3d electronic quadrupole transitions to chalcopyrite's unfilled d-like states (Belissont et al., 2016).

The right plot in Fig. 2 shows XAFS spectra measured in a suite of basaltic glasses. Lanzirotti et al. (2019) established that Cu K-edge XAFS spectra measured in S-free experimental glasses synthesized from basaltic starting materials at fO_2 between NNO-0.68 and NNO+4.7 (Fig. 2, right, upper two spectra) are consistent with stabilization of Cu^{1+}-oxide species. These spectra show the sharp, low-energy pre-edge peak (peak B) with intensities as high as the main absorption peak and attributed to 1s → 4p transitions. In these silicate glasses this is a signature of linearly coordinated Cu^{1+}-oxide species. Thus, we use XAFS measured from synthetic 1-atm sulfur-free, Kīlauea tholeiitic glass (NNO+4.7, Fig. 2 right, uppermost spectrum) as the predictor component for Cu–O species in the LCF analysis of the natural MI (as in Lanzirotti et al., 2019).

Lanzirotti et al. (2019) also showed that Cu XAFS from natural basaltic glasses equilibrated at $fO_2 <$ NNO with high sulfur contents (for example East Pacific Rise glasses, Fig. 2 right) most closely resemble the spectra measured for *CuS*, covellite. We therefore use XAFS measured from crystalline covellite (Fig. 2 left) as the LCF predictor component for Cu-S species (as in Lanzirotti et al., 2019).

However, the increased disorder in glasses often results in XAFS features that are broadened (with reduced peak intensities) when compared to comparable spectra measured in structured crystalline compounds. This makes it difficult to distinguish endmember Cu-S from Cu-Fe-S species in the natural MI. Therefore, although crystalline *CuS* XAFS is the best spectroscopic predictor for glass Cu sulfide species in the LCF fitting, this does not preclude that some fraction of sulfide-

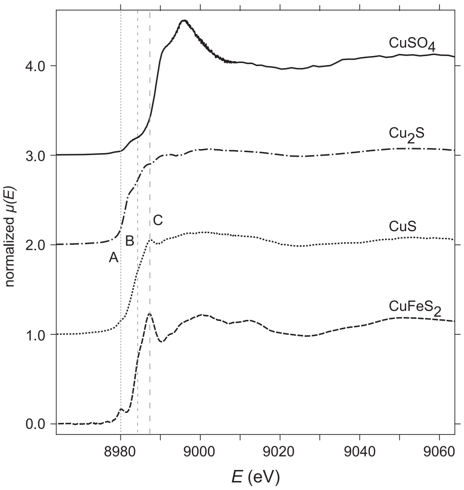

Fig. 2. Analyzed Cu K-edge XAFS spectra of selected Cu-bearing reference compounds (left) and synthetic and natural silicate glasses (right) from Lanzirotti et al. (2019). Spectra are offset vertically for clarity. (Left) Spectra measured in powdered anhydrous $CuSO_4$, chalcocite (Cu_2S), covellite (CuS), and chalcopyrite ($CuFeS_2$) standards. (Right) Spectra measured in sulfur-free experimental glass synthesized from basaltic starting material at NNO+4.7, olivine-hosted melt inclusions from 2013 and 2008 Kīlauea summit tephra, and glass from East Pacific Rise basalt. See text for description of spectral features marked as peaks A, B and C.

bound Cu is also bound to Fe (see section 5.2).

4. Results

4.1. Copper K-edge XAFS Measured in Synthetic Hydrous Andesitic Glasses

Spectroscopic analysis of synthetic andesitic glasses provides an opportunity to evaluate in more detail the relative roles of O, S and Cl in complexing Cu in basaltic and andesitic melts and provides an initial perspective of how Cu complexing may change under more oxidizing conditions (> NNO) relevant to arc magmatic systems. These synthetic glasses contain a restricted range of Cu concentrations (25–216 ppm) similar to the expected abundances for natural andesitic melts, but with highly variable S and Cl content and equilibrated over a broad range of fO_2 conditions (Zajacz et al., 2012) between ΔNNO of −1.2 and +1.8. Twelve synthetic glasses from the available suite were analyzed, and their S, Cu, and Cl abundances, fO_2, calculated Cu–O fraction and $S^{6+}/\Sigma S$ ratios are summarized in Table 2. Total Fe abundance (FeO^T) in the analyzed glasses is also shown, ranging from 4.0 – 7.9 wt% FeO^T. Measured S K-edge XAFS spectra for the S-bearing glasses are shown in Fig. 3, and Cu K-edge XAFS spectra for each of these glasses are shown in Fig. 4.

Glass G163 is the most reduced of the glasses analyzed, equilibrated at NNO-1.2 and containing 265 ppm S, 25 ppm Cu (Cu/S ratio of 0.09) and no Cl. S XAFS spectroscopy (Fig. 3) for G163 indicates that sulfide species dominate and the measured Cu XAFS (Fig. 4 top) are consistent with Cu-S. Nine glasses, samples G140, G142, G143, G155, G156, G157, G159, G160 and G161, were all equilibrated at an fO_2 of $\Delta NNO = -0.5$, but with variable amounts of S and Cl. This is an fO_2 similar to that at which MI glass from Kīlauea equilibrated. Of the nine glasses, five contain no S (G140, G142, G143, G157 and G160). Their Cu K-edge XAFS (Fig. 4 middle) show a prominent low energy peak at ~ 8984 eV consistent with Cu–O species being dominant (LCF calculated Cu–O fraction of > 0.90). The Cl abundance of these five S-free glasses is variable, with the highest concentration being 9974 ppm. Although their spectra remain consistent with Cu–O species being dominant, it is possible that there is a small systematic increase in edge-step normalized intensity (~ 0.14) as a function of increasing measured Cl abundance at an energy of ~ 8990 eV, which could indicate that some degree of Cl complexation with Cu is possible in these synthetic systems at high Cl concentrations (see Supplemental Document 1), significantly higher than what is expected in natural basaltic systems.

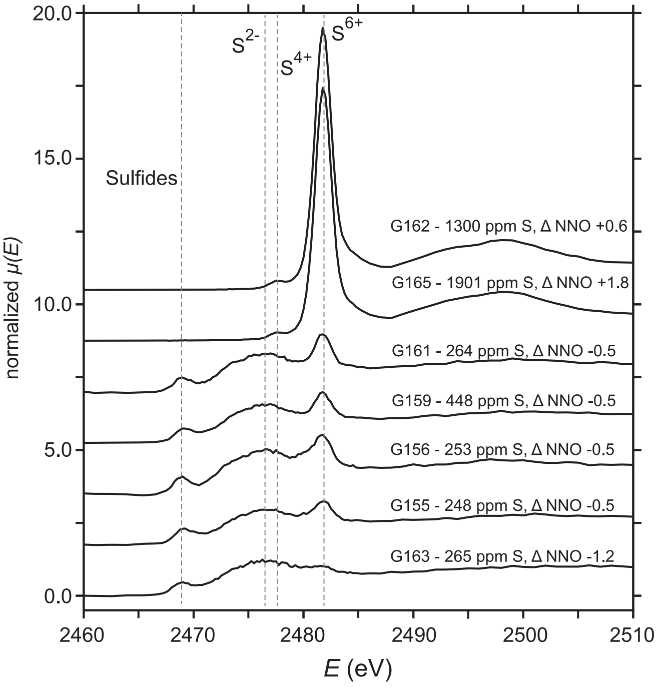

Fig. 3. Measured S K-edge XAFS spectra for the S-bearing synthetic glasses. Spectra are offset vertically for clarity. Dashed lines show energy positions of spectral features in silicate glasses considered diagnostic of sulfide, S^{2-}, S^{4+} and S^{6+} species. Annotated with measured S concentrations and fO_2.

Four of the glasses equilibrated at NNO-0.5 are S-bearing, with S concentrations of 248 – 448 ppm and Cu concentrations of 45–108 ppm (Cu/S ratios of 0.18–0.25). The S XAFS spectra (Fig. 3) of these four glasses indicates that they are dominated by sulfide ($S^{6+}/\Sigma S$ = 0.11—0.15), as expected at this fO_2, and their measured Cu XAFS (Fig. 4 middle) are consistent Cu-S (calculated Cu–O fraction of < 0.10). These four glasses also contain variable Cl (up to 10280 ppm), but in these samples no clear correlation is noted between Cl-free and Cl-rich glasses in normalized intensity measured at ~ 8990 eV.

Glasses G162 (NNO+0.6, 1300 ppm S, 216 ppm Cu, Cu/S ratio of 0.17) and G165 (NNO+1.84, 1901 ppm S, 25 ppm Cu, Cu/S ratio of

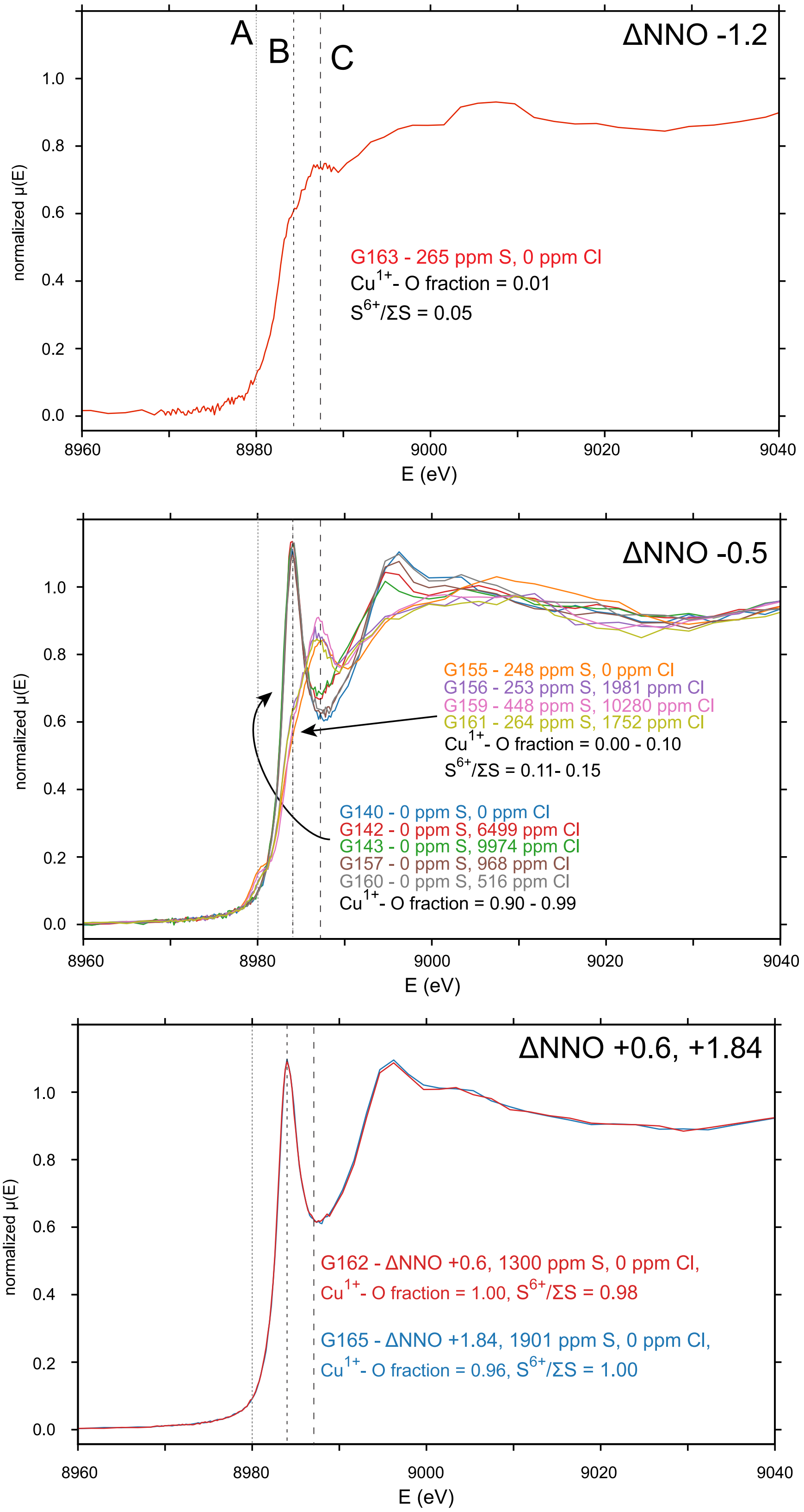

Fig. 4. Measured Cu K-edge XAFS spectra for the synthetic glasses synthesized at NNO-1.2 (top), NNO-0.5 (middle), and ΔNNO = +0.6 and +1.84 (bottom). Plots are annotated with measured S and Cl abundances, fO_2, and Cu–O fraction and $S^{6+}/\sum S$ ratios. See text for description of spectral features marked as peaks A, B and C.

0.14) are both S-bearing and equilibrated at fO_2's where sulfate is expected and confirmed with S XAFS (Fig. 3), yielding $S^{6+}/\Sigma S > 0.98$. Cu XAFS for these two glasses are similar (Fig. 4 bottom) and indicate that Cu–O species dominate (calculated Cu–O fraction > 0.96). No clear spectral contribution is observed in either of these two glasses from Cu-S or from Cu^{2+}-sulfate species.

What is apparent from the spectroscopic analysis of this suite of synthetic, hydrous andesitic glasses is that Cu-S species are preferentially stabilized in the melt when S^{2-} abundance is high relative to Cu. As S^{2-} concentrations decrease, Cu–O becomes dominant, even though total S concentrations are high, because the S is dominantly sulfate.

4.2. Copper K-edge XAFS Measured in Sulfate-Dominated Natural Glasses

Some example Cu K-edge XAFS spectra for naturally quenched MI are shown in Fig. 5, illustrating the differences observed in natural glasses with high (Fig. 5 left) and low (Fig. 5 right) calculated Cu–O fractions. The key distinguishing feature is that XAFS from high Cu-S glasses exhibit a peak at ~ 8987 eV (peak C), whereas high Cu–O glasses display a lower-energy pre-edge peak (peak B). Fig. 6 shows histograms of the calculated Cu–O fractions for the Kīlauea, Lassen and MGVF MI. The MGVF MI are dominated by the Cu–O component, with calculated Cu–O fraction between 0.68 and 0.91. The Lassen and Kīlauea MI show a more bimodal distribution of Cu–O and Cu-S species, with calculated Cu–O fraction between 0.14 and 0.77 for Lassen MI and between 0.18 and 0.78 for Kīlauea MI. The observed distribution of speciation in the Kīlauea MI is consistent with the results presented in Lanzirotti et al. (2019), where Cu–O dominant MI have low total S contents due to degassing (Thornber et al., 2015). The average S concentrations of Lassen and MGVF MI, however, are similar (1201 ± 275 (1σ) and 1390 ± 281 (1σ) ppm mean S abundance, respectively) and higher on average than that observed in Kīlauea MI (835 ± 341 (1σ) ppm mean S). Unlike Kīlauea MI, the total S abundances for MGVF MI do not show a correlation with the calculated Cu–O fraction (Fig. 7). Although the broad distribution in calculated Cu–O fraction observed in Lassen MI is similar to what is measured for Kīlauea MI, the observed spread is not as clearly correlated with measured total S. MGVF MI contain significantly more Cl on average (1662 ppm Cl) than is found in the Lassen MI (mean of 504 ppm Cl). Although Fe abundances have not been measured for all the MI analyzed spectroscopically, FeO^T values appear similar (Fig. 8). The average FeO^T for MGVF MI glasses is 6.69 wt%, 8.02 wt% for Lassen MI, and 10.75 wt % for Kīlauea MI. The synthetic andesitic glasses have the lowest average FeO^T of 5.5 wt%.

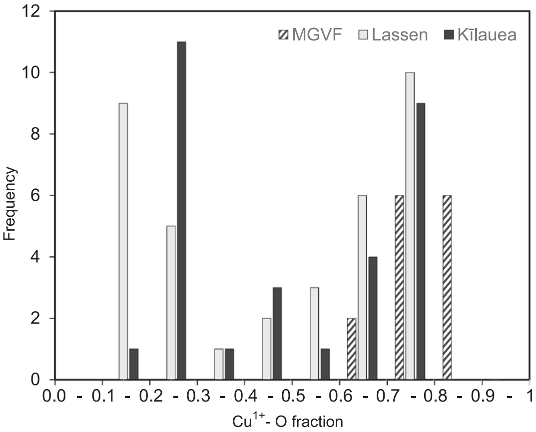

Fig. 6. Histograms of the calculated Cu–O fraction for the Kīlauea, Lassen and MGVF MI.

5. Discussion

5.1. The Relationship between Sulfur and Copper Speciation in Silicate Melts

The natural glasses analyzed in this study are all basaltic, olivine-hosted MI that were equilibrated over a broad range of fO_2's between roughly NNO-2 and NNO+2. The synthetic glasses are of hydrous andesitic composition, also synthesized at varying fO_2 but with variable S and Cl. For all glasses analyzed, the Cu K-edge XAFS spectroscopic analyses show that Cu-S species are preferentially stabilized in melts with high S^{2-}, relative to Cu, and that Cu–O species will dominate as the melt $[S^{2-}]$ decreases.

The Cu K-edge XAFS results for Kīlauea MI remain consistent with the observations made in Lanzirotti et al. (2019), showing that while both Cu–O and Cu-S species are stabilized in the melts, Cu–O species are preferentially stabilized in low-S MI whereas Cu-S species dominate in high-S MI. For the Kīlauea melts, equilibrated at $fO_2 <$ NNO, a transition between the two species is observed with increasing S concentrations. Although $S^{6+}/\Sigma S$ are not available for the Kīlauea MI analyzed here, previous studies have established that olivine-hosted MI from Kīlauea summit eruptions contain 5–20 % sulfate species (S^{6+}) (Lerner, 2020). If

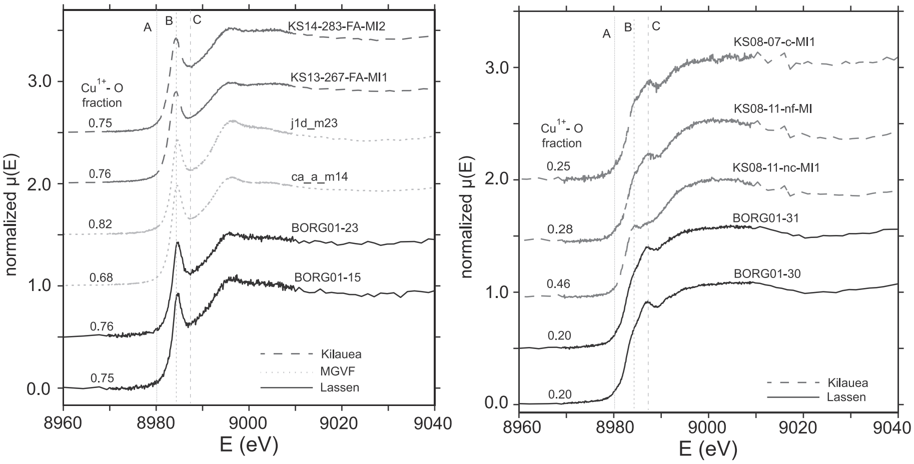

Fig. 5. Example Cu K-edge XAFS spectra of selected natural silicate glasses analyzed in this study with high (left, including Lassen, MGVF and Kīlauea) and low (right, including Lassen and Kīlauea) calculated Cu–O fractions. Spectra are offset vertically for clarity. The calculated Cu–O fraction for each glass is noted at the left of each spectrum and listed in Table 1. The spectrum from Kīlauea KS08-11-nc-MI (plotted to the right) has an intermediate Cu–O fraction for reference. The significance of the spectral features marked as peaks A, B and C is described in the text.

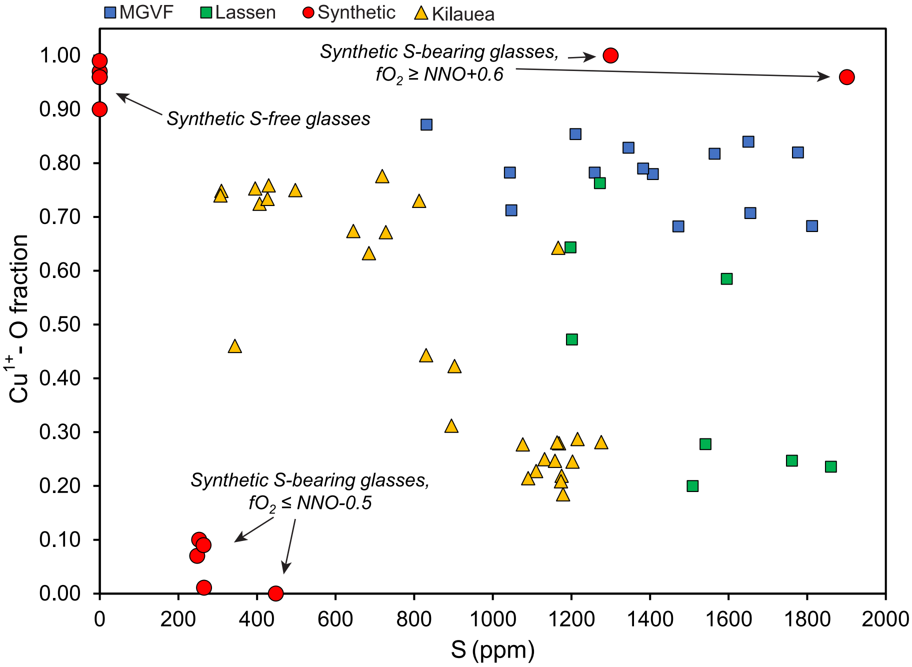

Fig. 7. Plot of measured total S concentration vs. Cu–O fraction for synthetic glasses and for the natural Lassen, MGVF, and Kīlauea MI.

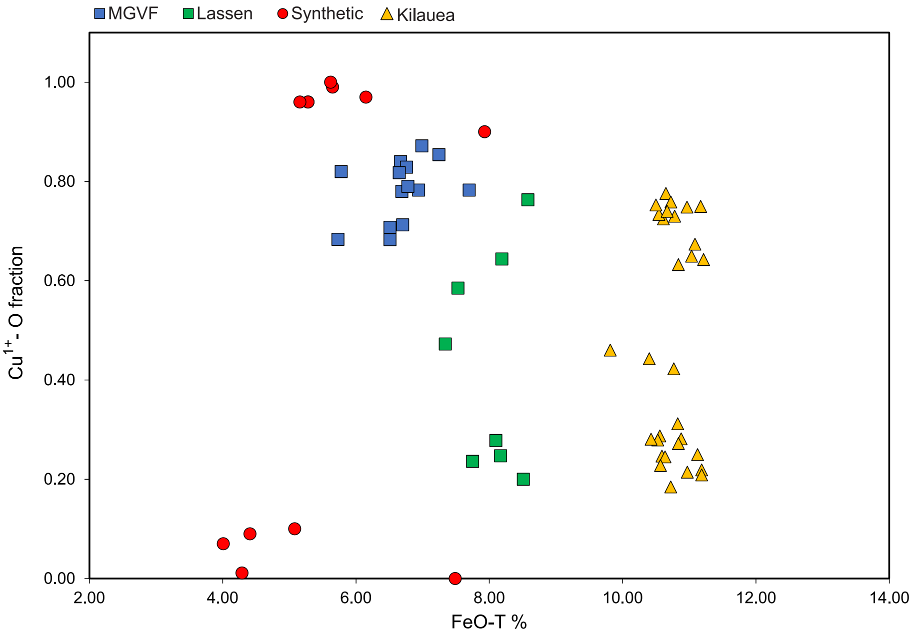

Fig. 8. Plot of measured FeO^T (weight %) vs. Cu–O fraction for synthetic glasses and for the natural MI from Lassen, MGVF, and Kīlauea.

we assume these Kīlauea MI have a fixed $S^{6+}/\Sigma S$ ratio of 0.18 (the mean value reported in Lerner, 2020), we calculate an estimated [S^{2-}] of ~ 200–1100 ppm for these glasses. For the Kīlauea MI, the observed relationship between Cu–O fraction and [S^{2-}] indicates that ~ 1000 ppm S^{2-} is required to stabilize a Cu–O fraction of ~ 0.25 (Fig. 9).

In contrast, Lassen and MGVF MI are equilibrated at fO_2's > NNO, where S^{6+} dominates (Fig. 1). The Cu XAFS results for these oxidized natural glasses also show that Cu–O species are stabilized as [S^{2-}] in the melt decreases, even though total S remains high because most of the dissolved S is present as S^{6+}. Based on measured $S^{6+}/\Sigma S$, Lassen MI have a maximum estimated [S^{2-}] of ~ 500 ppm (total S ~ 900–1900 ppm) and MGVF MI have estimated maximum [S^{2-}] ~ 300 ppm (total S ~ 800–1800 ppm). MGVF samples consistently yield the lowest estimated [S^{2-}] of the natural MI analyzed, with calculated Cu–O fraction of ~ 0.68–0.90 (Fig. 9). The Lassen MI display a range in calculated Cu–O fraction similar to that observed for Kīlauea MI, but the slope of the Cu–O fraction vs. [S^{2-}] relationship for Lassen MI is comparatively much steeper, requiring < 500 ppm [S^{2-}] to stabilize Cu–O fraction of ~ 0.25. In the synthetic, andesitic glasses, [S^{2-}] between 200 and 400 ppm appears sufficient for stabilizing Cu–O fraction of < 0.10 (Fig. 9).

For both the natural and synthetic systems studied here, as [S^{2-}] concentrations decrease, either because the total S content of the melt is low (for example due to S degassing, as is observed in many of the Kīlauea MI analyzed here) or because melt fO_2 stabilizes S^{6+} sulfate species preferentially to S^{2-} (as in the MGVF system), the speciation of Cu is increasingly dominated by Cu–O species. Over the fO_2 range where S

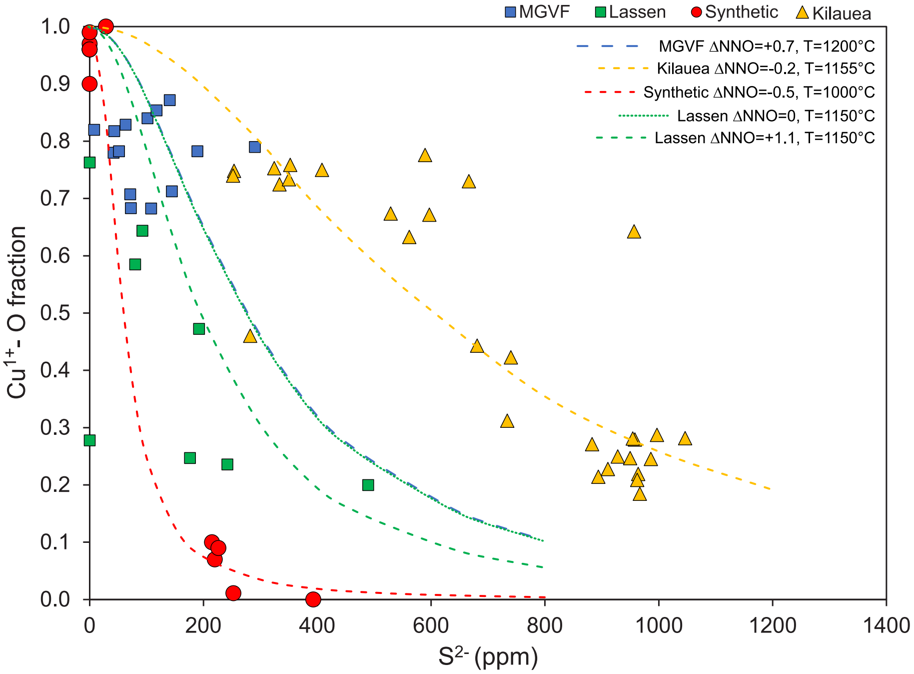

Fig. 9. Plot of estimated S^{2-} concentration (ppm) vs. Cu–O fraction for synthetic glasses and for the natural MI from Lassen, MGVF, and Kīlauea. The S^{2-} concentrations for the synthetic glasses and the Lassen and MGVF MI are calculated based on measured total S abundance and $S^{6+}/\sum S$ ratio. For the Kīlauea MI the S^{2-} concentrations are calculated based on measured total S abundance and assuming a fixed $S^{6+}/\Sigma S$ ratio of 0.18 on the basis of the mean value reported by Lerner (2020) for Kīlauea summit MI. Also shown are predicted Cu–O fractions for synthetic andesitic glasses, and Kīlauea, MGVF and BORG MI based on thermodynamic modeling of Cu speciation discussed in section 5.2 using equation (7) at the stated fO_2 and T conditions.

species are expected to transition from S^{2-} to S^{6+} (Fig. 1) (Jugo et al., 2010; Muth and Wallace, 2021; Nash et al., 2019; O'Neill, 2021), a transition in Cu speciation from Cu-S to Cu–O with increasing fO_2 is also discernable. This is likely coupled to the changing S speciation of the melt. However, the sensitivity of Cu–O fraction to $[S^{2-}]$ varies between the systems studied here, likely in response to the FeO abundance of the melt. Although Cu is strongly chalcophile, favoring the sulfide phase when compared to Fe, Fe concentrations in these basaltic melts are typically two orders of magnitude higher than those of Cu. Numerous studies have established that FeS is typically the most abundant dissolved sulfide species in mafic and andesitic melts (Mathez, 1976; Carroll and Rutherford, 1985; O'Neill and Mavrogenes, 2002; Moretti and Ottonello, 2003). It is therefore likely that S complexing by Fe imparts a compositional effect on the stabilized Cu–O fraction that is a function of the relative total S^{2-} and Fe concentrations in the melt. It would thus be expected that melts with higher Fe^{2+} will have lower amounts of freely available S^{2-} to complex with Cu^{1+}, even at more reduced fO_2 conditions below NNO, where sulfide species dominate. (Métrich et al., 2009; Jugo et al., 2010; Nash et al., 2019).

Exchange reactions that occur during quenching of silicate liquid can modify the valence of multivalent elements (Berry et al., 2003). A notable example is the electron exchange reaction between S and Fe described by (Métrich et al., 2009). With respect to Cu valence, Miller et al. (2024) suggest that an electron exchange reaction between Cu^{2+} and Fe^{2+} may occur on cooling that could result in some degree of Cu reduction:

$$Cu^{2+}O + Fe^{2+}O = Cu^{1+}O_{0.5} + Fe^{3+}O_{1.5} \quad (1)$$

However, given that our results show that Cu^{1+} species dominate in silicate melts equilibrated at fO_2's < NNO+2 and that a large change in coordination would be required to oxidize linear Cu^{1+} species to Cu^{2+}, the potential for noticeable changes to calculated Cu–O fraction on quenching due to such an electron exchange reaction for the samples studied is likely small.

It is unknown if Cu complexation may change upon quenching, particularly in hydrous glasses. For example, could Cu oxide species in MI react with available reduced S to form Cu sulfide species upon cooling? While this cannot be discounted as a possibility, the detection of Cu-S species in the experimental glasses, quenched within a few seconds to below the glass transition temperature, argues that such potential quench reactions are unlikely in the samples studied here.

5.2. *Thermodynamic Modeling of Cu Speciation in Silicate Melts*

The recognition that both Cu-S and Cu–O species are present in basaltic and andesitic melts, with Cu present in the 1+ state, and that their proportions depend on the concentration of $[S^{2-}]$ suggests the following equilibrium involving melt species may be applicable:

$$CuO_{0.5} + 0.25S_2 = CuS_{0.5} + 0.25O_2 \quad (2)$$

where $CuO_{0.5}$ and $CuS_{0.5}$ are species in the silicate melt. If the activity coefficients of $CuO_{0.5}$ and $CuS_{0.5}$ in the silicate melt are both equal to 1 or are constant over the range of composition, T and P for our samples, then an equilibrium expression at constant temperature can be written as:

$$\log\frac{[CuS_{0.5}]}{[CuO_{0.5}]} = \log K + 0.25\log f_{S_2} - 0.25\log f_{O_2} \quad (3)$$

where quantities in square brackets denote concentrations determined from LCF fitting. Strictly speaking, log *K* would be the equilibrium constant if the activity coefficients are both 1 or are of similar magnitude; if they had different magnitudes but remained constant, then Eq. (3) would yield log *K*', which would be the equilibrium constant modified by the activity coefficient ratio.

For the Kīlauea MI data, we calculated fS_2 values using sulfide capacities as described in O'Neill (2022). Values of fO_2 for the Kīlauea MI were assumed to be NNO-0.2 based on Helz et al. (2017). The range of temperatures inferred for the Kīlauea MI based on MgO-in-glass thermometry (Helz and Thornber, 1987) is 1137–1264 °C. Given this range, for fitting of the data we assumed that temperature was constant and therefore that *K* would also be constant. The Kīlauea data yielded a log *K* value of -1.93 ± 0.32 after removal of 4 data points that appeared to be outliers. Examination of the results, however, shows that Eq. (3) systematically misfits the Kīlauea MI data (Fig. 10 left), with residuals that depend strongly on melt total S concentration but show no relationship with the MgO-in-glass temperatures.

A possible explanation for this misfit could be that S concentrations in the melt affect the activity coefficients of $CuO_{0.5}$ and $CuS_{0.5}$ species in the silicate melt. However, this seems unlikely in light of Tuff and O'Neill's (2010) conclusion that the amount of S in silicate melts compared to oxygen is much too small to affect the activities of even the most chalcophile elements. Therefore, we conclude that Eq. (2) is not an accurate model for the Cu species in the melt.

Given the results shown in Fig. 8 that FeO^T or FeO variations in the melt might also affect speciation, we also tried the following Cu speciation equilibrium:

$$CuO_{0.5} + 0.5FeS = CuS_{0.5} + 0.5FeO \tag{4}$$

where all terms represent species in the silicate melt. This yields the equilibrium expression:

$$\log\frac{[CuS_{0.5}]}{[CuO_{0.5}]} = \log K + 0.5\log a_{FeS} - 0.5\log a_{FeO} \tag{5}$$

For the Kīlauea MI data, we calculated a_{FeO} values following O'Neill (2022). For calculation of a_{FeS} values, we could not use the method of O'Neill (2022) based on sulfide compositions because most melts had total S concentrations lower than calculated SCSS values, so we used an approximation described in Supplementary Document 2. Fitting of the Kīlauea data using Eq. (5) produced an identical misfit as that using Eq. (3) (Fig. 10 middle), again with residuals that are a strong function of dissolved S in the melt.

The two equilibria above involving melt species fail to accurately describe our data for proportions of Cu-S and Cu–O species in Kīlauea glasses. An alternative possibility is that Cu-S speciation in the melt also involves Fe:

$$CuO_{0.5} + Fe^{2+}O + S_2 = CuFe^{3+}S_2 + 0.75O_2 \tag{6}$$

where $CuO_{0.5}$, $Fe^{2+}O$ and $CuFe^{3+}S_2$ are species in the silicate melt, with the last of these species having the stoichiometry of chalcopyrite or high temperature intermediate solid solution. This yields the following equilibrium expression:

$$\log\frac{[CuFeS_2]}{[CuO_{0.5}]} = \log K + \log a_{FeO} + \log f_{S_2} - 0.75\log f_{O_2} \tag{7}$$

The Kīlauea data, again assuming a constant temperature, are well fit using Eq. (7) (Fig. 10 right), yielding a value for log *K* of -4.92 ± 0.20. The residuals to the model appear random and no longer depend on melt S concentration. Back calculation of the Kīlauea input data is reasonably good, but again with 4 data points that appear as outliers.

Next, we fit the experimental andesite glasses equilibrated at NNO-0.5, 1000 °C, and 200 MPa using Eq. (7) (Fig. 11 left). Given the lower temperature compared to the Kīlauea MI, we expected a different value for log *K* that would reflect the temperature dependence of Eq. (7). However, the results yielded a log *K* value of -4.75 ± 0.49, identical within uncertainty of the value determined for the Kīlauea data. This suggests little to no temperature dependence for the equilibrium constant for Eq. (6), though it is important to note that the values of a_{FeO}, fO_2 and fS_2 are temperature dependent. The value of log *K* for the combined Kīlauea and experimental andesite glass dataset is -4.88 ± 0.30. Model curves calculated using this value for the different compositions in our study are shown for comparison with the measured Cu–O fractions in Fig. 9. Our use of Eq. (7) helps to explain why the experimental andesite glasses at NNO-0.5 and $[S^{2-}]$ of 200–400 ppm are dominated by Cu-S species, whereas Kīlauea MI at similar relative fO_2 and $[S^{2-}]$ are dominated by Cu–O (Fig. 9). Although the two datasets are at similar relative fO_2 values, the lower temperature of the experimental andesite glasses gives them lower absolute fO_2 values, which causes Eq. (6) to shift to the right, favoring the $CuFe^{3+}S_2$ species despite similar $[S^{2-}]$ values.

We used the value for log *K* of the combined Kīlauea and andesite glass dataset to calculate the predicted Cu–O fraction for the MGVF melt inclusions (Fig. 11 middle), which equilibrated at fO_2's > NNO, where S^{6+} dominates. The results suggest that speciation of Cu as a $CuFeS_2$ melt species is accurately described by Eq. (6) at higher fO_2 values, though for many of the samples, the predicted Cu–O fraction is slightly higher than the measured value. Application to the Lassen MI dataset results in poor agreement between predicted and measured Cu–O fractions, except for one sample with a low measured Cu–O fraction (Fig. 11 right). In all other samples, however, the predicted values of Cu–O fraction are significantly higher. The Lassen MI have broadly similar temperature, composition, fO_2, and melt S as the MGVF MI, and predicted Cu–O fractions for the two sample suites are fairly similar (see model curves in

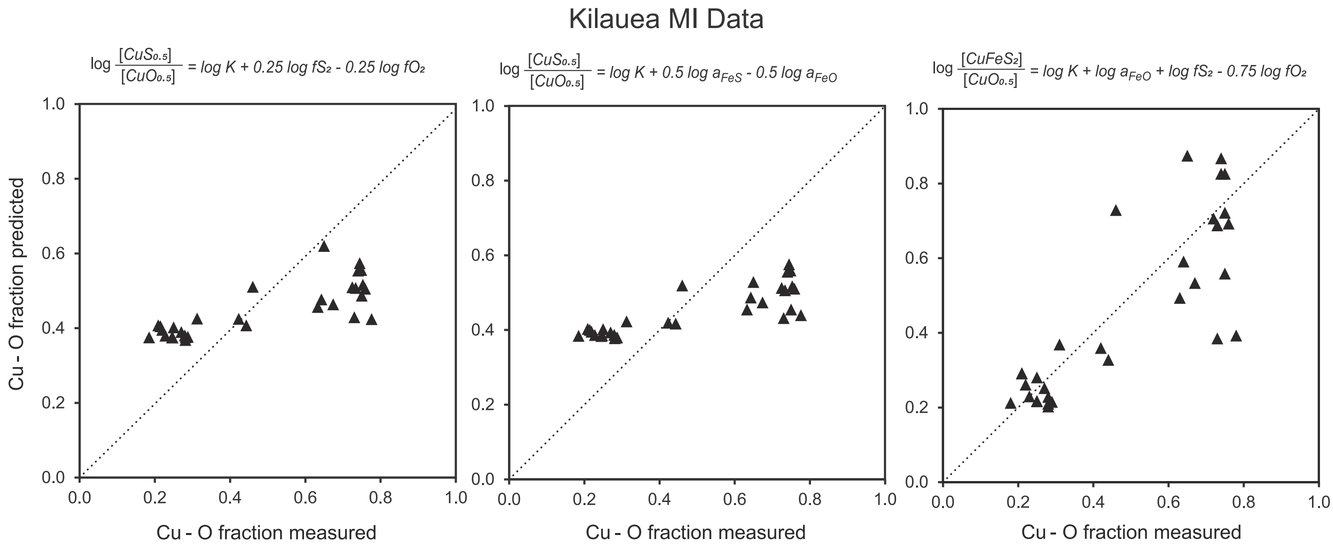

Fig. 10. Comparison of predicted vs measured Cu–O fraction for Kīlauea MI based on thermodynamic modeling of Cu speciation using equation (3) (left), equation (5) (middle) and equation (7) (right).

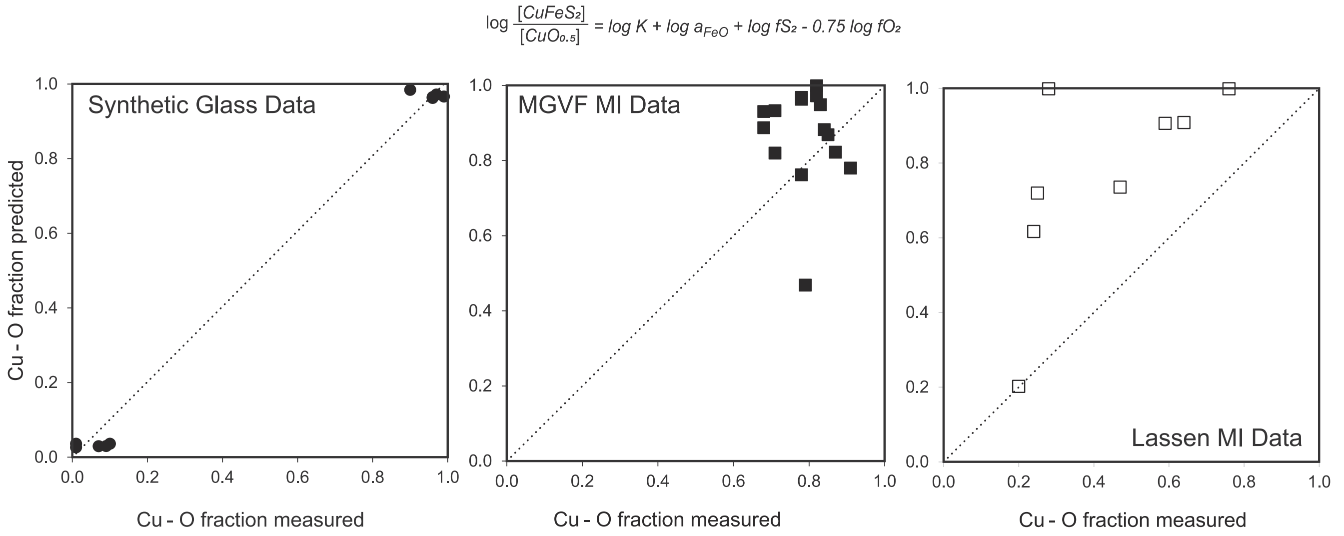

Fig. 11. Comparison of predicted vs measured Cu–O fraction for synthetic andesitic glasses (left) and MGVF (middle) and Lassen (right) MI based on thermodynamic modeling of Cu speciation using equation (7). The log *K* value used for the andesite glasses was derived based solely on those experiments, as discussed in the text. The log *K* value used for the MGVF and Lassen MI data is based on the combined Kīlauea MI and andesite dataset.

Fig. 9). Given these results, it seems possible that the Cu–O fractions in many of the Lassen samples were affected by some kind of quenching or other disequilibrium effect.

5.3. *Implications for Cu Solubility and Partitioning*

The recognition that both Cu-S and Cu–O species can be stabilized in basaltic and andesitic melts, and may co-exist dependent on the amount of available S^{2-}, has potential implications for understanding Cu partitioning in magmatic systems. For example, the equilibrium partitioning between dissolved Cu in the melt and Cu-Fe sulfides will be dependent on the speciation of Cu dissolved in the melt. Simon et al. (2006) postulated the following possible equilibrium between Cu in the melt (*m*) and in sulfide phases (in this case possible pyrrhotite, designated *po*) where Cu–O species are stabilized:

$$CuO_{0.5}^{m} + FeS^{po} + 0.5S_2 = CuFeS_2^{po} + 0.25O_2 \qquad (8)$$

whereas in melts where Cu is speciated as sulfide, the equilibrium reaction would be rewritten as:

$$CuS_{0.5}^{m} + FeS^{po} + 0.25S_2 = CuFeS_2^{po} \qquad (9)$$

such that the partitioning of Cu between melt and sulfide varies with melt fO_2 and fS_2. The thermodynamic modeling of our results suggests a modified version of Eq. (9) with a $CuFeS_2$ melt species would be appropriate. The partitioning of Cu between melt and vapor phases may have similar dependencies, which could be important for understanding metal enrichment potential in exsolved fluids (Berry et al., 2006, 2009) or with respect to volcanic degassing to the atmosphere (Edmonds et al., 2018; Zelenski et al., 2021).

Our results are also consistent with studies that have shown that Cu^{1+} species dominate in terrestrial silicate melts at crustal pressures, even in the relatively oxidizing, water-rich conditions of arc basalts and andesites (Candela and Holland, 1984; Ripley and Brophy, 1995; Liu et al., 2024; Miller et al., 2024). This result implies that melt Cu valence alone cannot explain the sulfide-melt Cu isotope fractionation inferred from lower crustal data (e.g. Liu et al., 2023; Zou et al., 2024). However, this does not exclude the possibility that melt oxidation state influences Cu isotope behavior. The transition from Cu-S to Cu–O as a function of the melt oxidation state may drive differences in Cu isotope behavior within reduced (e.g., mid-ocean ridge magmas) and oxidized (e.g., arc magma) systems.

6. Conclusions

Cu K-edge XAFS data have been collected from a suite of natural and synthetic silicate glasses to better understand Cu speciation in basaltic and andesitic magmas. Samples analyzed include olivine-hosted MI from tephras in the Lassen and Michoacán-Guanajuato volcanic fields, both of which are representative of natural melts equilibrated at $fO_2 > NNO$. Sampled MI from summit eruptions at Kīlauea Volcano were analyzed as being representative of basaltic melts equilibrated at $fO_2 < NNO$. Also analyzed were S-bearing and S-free experimental glasses of andesitic composition equilibrated at varying fO_2's. The spectroscopic data from all glasses analyzed, both natural and synthetic, consistently show that as concentrations of dissolved melt sulfide decrease, the dissolved Cu species in the melt evolve from dominantly Cu-sulfide to Cu-oxide. At intermediate S^{2-} abundances both Cu species appear to coexist. The sensitivity of the transition from Cu-sulfide to Cu-oxide species as a function of total dissolved S^{2-} also appears dependent on FeO abundance, possibly because higher amounts of Fe^{2+} lower the amount of S^{2-} freely available to complex with Cu^{1+}.

Several magmatic processes can modify dissolved melt S^{2-} content and thus affect which Cu species are stabilized. For example, in the Kīlauea samples the transition from Cu-S to Cu–O species correlates with observed trends attributed to the degree of low pressure S degassing from the magma chamber between 2008 and 2018 (Thornber et al., 2015; Lanzirotti et al., 2019). Similarly, it is well-established that when melt fO_2 increases above ~ NNO, stabilized S species transition from S^{2-} to S^{6+}. The analyzed MI from MGVF appear to have equilibrated at fO_2's between NNO+0.5 and NNO+1.7 and, as expected for such fO_2's, S^{6+} is the dominant S species. In these MI, Cu–O species dominate even though total S abundances are relatively high. Our results show that a transition in Cu speciation from Cu-S to Cu–O occurs over a roughly similar range in fO_2 as the transition from S^{2-} to S^{6+} in both the natural and synthetic samples analyzed. This is, again, a consequence of the decreased availability of S^{2-}.

Thermodynamic modeling of Cu speciation in the glasses we studied suggests that speciation of Cu as a $CuFeS_2$ melt species (similar to chalcopyrite or intermediate solid solution) most accurately predicts the measured Cu species. The modeling suggests that a_{FeO} in the silicate melt, fO_2 and melt S^{2-} (expressed as fS_2) are the most important parameters controlling the proportions of Cu–O vs. Cu-S species. Our results show no indication of a temperature dependence to the melt speciation equilibrium, but these key controlling parameters are themselves all temperature dependent. Our thermodynamic analysis allows for prediction of the Cu–O fraction in silicate melts of basaltic to andesitic composition.

Our results emphasize the utility of spectroscopic data collected from hydrous silicate glasses synthesized at relevant geologic conditions with S. Although experimentally challenging to synthesize, these materials provide critical data for helping understand the controls on the speciation of chalcophile elements in silicate melts.

CRediT authorship contribution statement

Antonio Lanzirotti: Writing – original draft, Validation, Project administration, Methodology, Investigation, Funding acquisition, Formal analysis, Data curation, Conceptualization. **Michelle Muth:** Writing – original draft, Resources, Formal analysis, Conceptualization. **Elisabet Head:** Writing – original draft, Validation, Resources, Methodology, Investigation, Funding acquisition, Formal analysis, Conceptualization. **Matthew Newville:** Software, Methodology, Investigation, Formal analysis, Data curation. **Molly McCanta:** Writing – review & editing, Funding acquisition. **Paul J. Wallace:** Writing – original draft, Resources, Funding acquisition, Conceptualization. **Zoltan Zajacz:** Writing – review & editing, Writing – original draft, Resources, Conceptualization.

Data availability

Data are available through the NSF Synchrotron Earth and Environmental Science (SEES) data repository site at https://doi.org/10.71622/332x-t833.

Declaration of competing interest

The authors declare that they have no known competing financial interests or personal relationships that could have appeared to influence the work reported in this paper.

Acknowledgements

This study was funded by a National Science Foundation Earth Sciences collaborative research grant to A. Lanzirotti, E. Head, M. McCanta and P. Wallace (EAR- 1834930, 1834941, 1834959, 1834939). XAFS spectroscopy data were collected at GeoSoilEnviroCARS (Sector 13), Advanced Photon Source (APS), Argonne National Laboratory. GeoSoilEnviroCARS is supported by the National Science Foundation, Earth Sciences (EAR-1128799) and Department of Energy, Geosciences (DE-FG02-94ER14466). Use of the Advanced Photon Source was supported by the U.S. Department of Energy, Office of Science, Office of Basic Energy Sciences, under contract no. DE-AC02-06CH11357. We acknowledge the Smithsonian Institute National Museum of Natural History Department of Mineral Sciences for the use of NMNH 117393 basalt reference glasses for this study. We acknowledge Lopaka Lee and the Hawaiian Volcano Observatory (US Geological Survey) for providing Kīlauea materials for study and for constructive discussions. We thank Xingcheng Liu, an anonymous reviewer, and Associate Editor Georges Calas for constructive comments that helped improve the final manuscript.

Appendix A. Supplementary material

Supplemental Table 1: Description of analyzed Kīlauea samples. Supplemental Document 1: Discussion of the Relationship Between Chlorine and Copper Speciation in Silicate Melts Studied. Supplementary Document 2: Details of thermodynamic modeling. Supplementary material to this article can be found online at https://doi.org/10.1016/j.gca.2025.02.037.

References

Beermann, O., Botcharnikov, R.E., Holtz, F., Diedrich, O., Nowak, M., 2011. Temperature dependence of sulfide and sulfate solubility in olivine-saturated basaltic magmas. *Geochim. Cosmochim. Acta* 75, 7612–7631.

Belissont, R., Munoz, M., Boiron, M.-C., Luais, B., Mathon, O., 2016. Distribution and oxidation state of Ge, Cu and Fe in sphalerite by μ-XRF and K-edge μ-XANES: insights into Ge incorporation, partitioning and isotopic fractionation. *Geochim. Cosmochim. Acta* 177, 298–314.

Berry, A.J., Hack, A.C., Mavrogenes, J.A., Newville, M., Sutton, S.R., 2006. A XANES study of Cu speciation in high-temperature brines using synthetic fluid inclusions. Am. Mineral. 91, 1773–1782.

Berry, A.J., Harris, A.C., Kamenetsky, V.S., Newville, M., Sutton, S.R., 2009. The speciation of copper in natural fluid inclusions at temperatures up to 700 °C. *Chem. Geol.* 259, 2–7.

Berry, A.J., Shelley, J.M.G., Foran, G.J., O'Neill, H.S.C., Scott, D.R., 2003. A furnace design for XANES spectroscopy of silicate melts under controlled oxygen fugacities and temperatures to 1773 K. *J. Synchrotron Radiat.* 10, 332–336.

Candela, P.A., Holland, H.D., 1984. The partitioning of copper and molybdenum between silicate melts and aqueous fluids. *Geochim. Cosmochim. Acta* 48, 373–380.

Carroll, M.R., Rutherford, M.J., 1985. Sulfide and sulfate saturation in hydrous silicate melts. *J. Geophys. Res. Solid Earth* 1978–2012 (90), C601–C612.

Chen, Z., Chen, J., Tamehe, L.S., Zhang, Y., Zeng, Z., Xia, X., Cui, Z., Zhang, T., Guo, K., 2022. Heavy Copper Isotopes in Arc-Related Lavas From Cold Subduction Zones Uncover a Sub-Arc Mantle Metasomatized by Serpentinite-Derived Sulfate-Rich Fluids. *J. Geophys. Res. Solid Earth* 127, e2022JB024910.

Cottrell, E., Lanzirotti, A., Mysen, B., Birner, S., Kelley, K., Botcharnikov, R., Davis, F., Newville, M., 2018. A Mössbauer-based XANES calibration for hydrous basalt glasses reveals radiation-induced oxidation of Fe. *Am. Mineral.* 103, 489–501.

Edmonds, M., Mather, T.A., Liu, E.J., 2018. A distinct metal fingerprint in arc volcanic emissions. *Nat. Geosci.* 11, 790.

Fulton, J.L., Hoffmann, M.M., Darab, J.G., 2000. An X-ray absorption fine structure study of copper (I) chloride coordination structure in water up to 325 C. *Chem. Phys. Lett.* 330, 300–308.

Gaetani, G.A., Grove, T.L., 1997. Partitioning of moderately siderophile elements among olivine, silicate melt, and sulfide melt: constraints on core formation in the Earth and Mars. *Geochim. Cosmochim. Acta* 61, 1829–1846.

Goh, S.W., Buckley, A.N., Lamb, R.N., Rosenberg, R.A., Moran, D., 2006. The oxidation states of copper and iron in mineral sulfides, and the oxides formed on initial exposure of chalcopyrite and bornite to air. *Geochim. Cosmochim. Acta* 70, 2210–2228.

Helz, R.T., Cottrell, E., Brounce, M.N., Kelley, K.A., 2017. Olivine-melt relationships and syneruptive redox variations in the 1959 eruption of Kīlauea Volcano as revealed by XANES. *J. Volcanol. Geotherm. Res.* 333–334, 1–14.

Helz, R.T., Thornber, C.R., 1987. Geothermometry of Kilauea Iki lava lake. Hawaii. *Bull. Volcanol.* 49, 651–668.

Holzheid, A., Lodders, K., 2001. Solubility of copper in silicate melts as function of oxygen and sulfur fugacities, temperature, and silicate composition. *Geochim. Cosmochim. Acta* 65, 1933–1951.

Johnson, E.R., Wallace, P.J., Delgado, G.H., Manea, V.C., Kent, A.J.R., Bindeman, I.N., Donegan, C.S., 2009. Subduction-related Volatile Recycling and Magma Generation beneath Central Mexico: Insights from Melt Inclusions, Oxygen Isotopes and Geodynamic Models. *J. Petrol.* 50, 1729–1764.

Jugo, P.J., 2009. Sulfur content at sulfide saturation in oxidized magmas. *Geology* 37, 415–418.

Jugo, P.J., Wilke, M., Botcharnikov, R.E., 2010. Sulfur K-edge XANES analysis of natural and synthetic basaltic glasses: Implications for S speciation and S content as function of oxygen fugacity. *Geochim. Cosmochim. Acta* 74, 5926–5938.

Kau, L.S., Spira-Solomon, D.J., Penner-Hahn, J.E., Hodgson, K.O., Solomon, E.I., 1987. X-ray absorption edge determination of the oxidation state and coordination number of copper. Application to the type 3 site in Rhus vernicifera laccase and its reaction with oxygen. *J. Am. Chem. Soc.* 109, 6433–6442.

Kraft, S., Stümpel, J., Becker, P., Kuetgens, U., 1996. High resolution x-ray absorption spectroscopy with absolute energy calibration for the determination of absorption edge energies. *Rev. Sci. Instrum.* 67, 681–687.

Kress, V.C., Carmichael, I.S., 1991. The compressibility of silicate liquids containing Fe_2O_3 and the effect of composition, temperature, oxygen fugacity and pressure on their redox states. *Contrib. Mineral. Petrol.* 108, 82–92.

Lanzirotti, A., Lee, L., Head, E., Sutton, S.R., Newville, M., McCanta, M., Lerner, A.H., Wallace, P.J., 2019. Direct measurements of copper speciation in basaltic glasses: understanding the relative roles of sulfur and oxygen in copper complexation in melts. *Geochim. Cosmochim. Acta* 267, 164–178.

Lerner, A.H., 2020. The depths and locations of magma reservoirs and their consequences for the behavior of sulfur and volcanic degassing. University of Oregon. Ph.D. Dissertation.

Lerner, A.H., Muth, M.J., Wallace, P.J., Lanzirotti, A., Newville, M., Gaetani, G.A., Chowdhury, P., Dasgupta, R., 2021a. Improving the reliability of Fe-and S-XANES measurements in silicate glasses: correcting beam damage and identifying Fe-oxide nanolites in hydrous and anhydrous melt inclusions. *Chem. Geol.* 586, 120610.

Lerner, A.H., Wallace, P.J., Shea, T., Mourey, A.J., Kelly, P.J., Nadeau, P.A., Elias, T., Kern, C., Clor, L.E., Gansecki, C., 2021b. The petrologic and degassing behavior of sulfur and other magmatic volatiles from the 2018 eruption of Kīlauea, Hawai'i: melt concentrations, magma storage depths, and magma recycling. *Bull. Volcanol.* 83, 43.

Liu, S.-A., Rudnick, R.L., Liu, W.-R., Teng, F.-Z., Wu, T.-H., Wang, Z.-Z., 2023. Copper isotope evidence for sulfide fractionation and lower crustal foundering in making continental crust. *Sci. Adv.* 9, eadg6995.

Liu, X., Xiong, X., Audétat, A., Li, Y., Song, M., Li, L., Sun, W., Ding, X., 2014. Partitioning of copper between olivine, orthopyroxene, clinopyroxene, spinel, garnet and silicate melts at upper mantle conditions. *Geochim. Cosmochim. Acta* 125, 1–22.

Liu, X., Zhang, L., Zhu, S., Li, L., Xiong, X., 2024. Oxidation state of Cu in silicate melts at upper mantle conditions. *Sci. Rep.* 14, 5802.

Mathez, E.A., 1976. Sulfur solubility and magmatic sulfides in submarine basalt glass. *J. Geophys. Res.* 81, 4269–4276.

Matjuschkin, V., Blundy, J.D., Brooker, R.A., 2016. The effect of pressure on sulphur speciation in mid- to deep-crustal arc magmas and implications for the formation of porphyry copper deposits. *Contrib. Mineral. Petrol.* 171, 66.

Métrich, N., Berry, A.J., O'Neill, H.S.C., Susini, J., 2009. The oxidation state of sulfur in synthetic and natural glasses determined by X-ray absorption spectroscopy. *Geochim. Cosmochim. Acta* 73, 2382–2399.

Miller, L.A., Berry, A.J., O'Neill, H.S.C., Wykes, J., Newville, M., Lanzirotti, T., 2024. The effect of composition, temperature and pressure on the oxidation state and coordination environment of copper in silicate melts. *Geochim. Cosmochim. Acta* 364, 129–147.

Moretti, R., Ottonello, G., 2003. Polymerization and disproportionation of iron and sulfur in silicate melts: insights from an optical basicity-based approach. *J. Non-Cryst. Solids* 323, 111–119.

Muth, M.J., Cottrell, E., 2023. No detectable redox exchange between sulfur and iron during rapid cooling of basalts. *Earth Planet. Sci. Lett.* 616, 118210.

Muth, M.J., Wallace, P.J., 2021. Slab-derived sulfate generates oxidized basaltic magmas in the southern Cascade arc (California, USA). *Geology* 49, 1177–1181.

Muth, M.J., Wallace, P.J., 2022. Sulfur recycling in subduction zones and the oxygen fugacity of mafic arc magmas. *Earth Planet. Sci. Lett.* 599, 117836.

Nash, W.M., Smythe, D.J., Wood, B.J., 2019. Compositional and temperature effects on sulfur speciation and solubility in silicate melts. *Earth Planet. Sci. Lett.* 507, 187–198.

Newville, M., 2013. Larch: An Analysis Package for XAFS and Related Spectroscopies. *J. Phys. Conf. Ser.* 430, 012007.

O'Neill, H.S.C., 2022. The thermodynamic controls on sulfide saturation in silicate melts with application to ocean floor basalts. *Magma Redox Geochem.*, 177–213.

O'Neill, H.S.C., 2019. Comment on "Compositional and temperature effects on sulfur speciation and solubility in silicate melts" by Nash et al. [Earth Planet. Sci. Lett. 507 (2019) 187-198]. Earth Planet. Sci. Lett. 560, 116843.

O'Neill, H.S.C., Mavrogenes, J.A., 2002. The sulfide capacity and sulfur content at sulfide saturation of silicate melts at 1400 C and 1 bar. *J. Petrol.* 43, 1049–1087.

Pearce, C.I., Pattrick, R.A.D., Vaughan, D.J., Henderson, C.M.B., Van der Laan, G., 2006. Copper oxidation state in chalcopyrite: Mixed Cu d9 and d10 characteristics. *Geochim. Cosmochim. Acta* 70, 4635–4642.

Poland, M., Miklius, A., Orr, T., Sutton, J., Thornber, C., Wilson, D., 2008. New episodes of volcanism at Kilauea Volcano. Hawaii. *Eos Trans. Am. Geophys. Union* 89, 37–38.

Ripley, E.M., Brophy, J.G., 1995. Solubility of copper in a sulfur-free mafic melt. *Geochim. Cosmochim. Acta* 59, 5027–5030.

Ripley, E.M., Brophy, J.G., Li, C., 2002. Copper solubility in a basaltic melt and sulfide liquid/silicate melt partition coefficients of Cu and Fe. *Geochim. Cosmochim. Acta* 66, 2791–2800.

Simon, A.C., Pettke, T., Candela, P.A., Piccoli, P.M., Heinrich, C.A., 2006. Copper partitioning in a melt–vapor–brine–magnetite–pyrrhotite assemblage. *Geochim. Cosmochim. Acta* 70, 5583–5600.

Sutton, S.R., Rivers, M.L., Chariton, S., Eng, P.J., Lanzirotti, A., Newville, M., Officer, T., Prakapenka, V.B., Ryu, Y.J., Stubbs, J.E., 2022. GeoSoilEnviroCARS (Sector 13) at the Advanced Photon Source: a comprehensive synchrotron radiation facility for Earth science research at ambient and extreme conditions. *Phys. Chem. Miner.* 49, 32.

Thornber, C.R., Orr, T.R., Heliker, C., Hoblitt, R.P., 2015. Petrologic testament to changes in shallow magma storage and transport during 30+ years of recharge and eruption at Kılauea Volcano, Hawai 'i. *Hawaii. Volcanoes Source Surf.* 208, 147.

Tuff, J., O'Neill, H.S.C., 2010. The effect of sulfur on the partitioning of Ni and other first-row transition elements between olivine and silicate melt. *Geochim. Cosmochim. Acta* 74, 6180–6205.

Vegelius, J.R., Kvashnina, K.O., Hollmark, H., Klintenberg, M., Kvashnin, Y.O., Soroka, I. L., Werme, L., Butorin, S.M., 2012. X-ray Spectroscopic Study of Cu_2S, CuS, and Copper Films Exposed to Na_2S Solutions. *J. Phys. Chem. C* 116, 22293–22300.

Zajacz, Z., Candela, P.A., Piccoli, P.M., Sanchez-Valle, C., Wälle, M., 2013. Solubility and partitioning behavior of Au, Cu, Ag and reduced S in magmas. *Geochim. Cosmochim. Acta* 112, 288–304.

Zajacz, Z., Candela, P.A., Piccoli, P.M., Wälle, M., Sanchez-Valle, C., 2012. Gold and copper in volatile saturated mafic to intermediate magmas: Solubilities, partitioning, and implications for ore deposit formation. *Geochim. Cosmochim. Acta* 91, 140–159.

Zelenski, M., Simakin, A., Taran, Y., Kamenetsky, V., Malik, N., 2021. Partitioning of elements between high-temperature, low-density aqueous fluid and silicate melt as derived from volcanic gas geochemistry. *Geochim. Cosmochim. Acta* 295, 112–134.

Zhang, H.L., Cottrell, E., Solheid, P.A., Kelley, K.A., Hirschmann, M.M., 2018. Determination of Fe3+/ΣFe of XANES basaltic glass standards by Mössbauer spectroscopy and its application to the oxidation state of iron in MORB. *Chem. Geol.* 479, 166–175.

Zou, Z., Wang, Z., Xu, Y.-G., Ciazela, J., Wang, X., Foley, S., Zhang, W.-Q., Li, W., Li, M., Liu, Y., 2024. Contrasting Cu isotopes in mid-ocean ridge basalts and lower oceanic crust: Insights into the oceanic crustal magma plumbing systems. *Earth Planet. Sci. Lett.* 627, 118563.